DC magnetron sputter deposition in pure helium gas: formation of porous films or gas/solid nanocomposite coatings

Sara Ibrahim, Asunción Fernández, Pascal Brault, Audrey Sauldubois, Pierre Desgardin, Amael Caillard, Dirk Hufschmidt, Maria-Carmen Jiménez de Haro, Thierry Sauvage, Marie-France Barthe, et al.

DC magnetron sputter deposition in pure helium gas: formation of porous films or gas/solid nanocomposite coatings

Sara Ibrahim[a], Asunción Fernández [a,b], Pascal Brault[a], Audrey Sauldubois [a], Pierre Desgardin[c], Amael Caillard[a], Dirk Hufschmidt[b], Maria-Carmen. Jiménez de Haro[b], Thierry Sauvage [c], Marie-France Barthe[c] and Anne-Lise Thomann[a,*]

[a] GREMI, UMR7344 CNRS Université d'Orléans, 14 rue d'Issoudun, 45067 Orléans, France

[b] Instituto de Ciencia de Materiales de Sevilla, CSIC-Univ. Seville, Avda. Américo Vespucio 49, 41092 Seville, Spain

[c] CEMHTI, UPR3079 CNRS, 1D avenue de la Recherche Scientifique, 45071 Orléans, France

sara.ibrahim@univ-orleans.fr

asuncion@icmse.csic.es

pascal.brault@univ-orleans.fr

audrey.sauldubois@univ-orleans.fr

pierre.desgardin@cnrs-orleans.fr

amael.caillard@univ-orleans.fr

dirk@icmse.csic.es

cjimenez@icmse.csic.es

thierry.sauvage@cnrs-orleans.fr

marie-france.barthe@cnrs-orleans.fr

*Corresponding author : anne-lise.thomann@univ-orleans.fr

Tel : +33 (0)2 38 49 48 70

Abstract

Magnetron sputtering of two materials (Aluminum and Silicon) was performed in He gas and led to the formation of very different porous thin films: a fiberform nanostructure or a gas/solid nanocomposite. The composition of the thin films obtained was analyzed by means of ion beam techniques: Rutherford backscattering and proton elastic backscattering spectroscopies to measure the amount of Al(Si) deposited atoms and that of He atoms inserted inside the films. Microstructural and crystalline properties were analyzed by scanning electron microscopy and X-ray diffraction. Transmission electron microscopy coupled with electron energy loss spectroscopy were used to investigate the presence of empty or He filled pores or even bubbles. Correlating the Al(Si) film properties with the deposition conditions evaluated by SRIM (sputtering process at the target) and by a homemade collision code (species transport to the substrate) gave a better insight into the reason for the formation of such different films. The role of both He ions backscattered at the target and surface mobility during the growth is discussed. Comparison with low kinetic energy He+ implantation experiments indicates that similar mechanisms, such as He insertion, diffusion inside the lattice, release or accumulation into pores and bubbles, are certainly taking place

Keywords

DC magnetron sputtering in helium, nanostructured thin films, porous thin film, gas trapped in thin film, solid/gas nano-composites

1. Introduction

The design of porous and nanostructured materials has been of great interest to the materials science community over the last decades, since nanostructures modify the material's properties, increase the exchange surface and bring significant improvements in different applications. The fabrication of nanostructured thin films has enhanced the performance of numerous technological devices dedicated to energy generation and storage, optics, microelectronics, catalysis etc. [1-3].

Magnetron sputter deposition is a versatile technique that enables 100 nm to a few µm thick films of a large range of elements and compounds to be manufactured. Widely used in industry, this technique also has the advantage of controlling the film microstructure and porosity by playing with different parameters (pressure, target-to-substrate distance etc.) or by working in different regimes (DC, pulsed DC, HiPIMS…) [4,5]. One way to obtain porous films is to work in a geometric configuration ensuring a very small angle between the incoming atom flux direction and the substrate surface. This so-called glancing angle deposition (GLAD) technique enables the growth of nanostructured films in the form of inclined columns, zigzag columns, nano-spirals, nanotubes and branched nano columns, depending on the experimental conditions such as the substrate temperature, the gas pressure, the substrate tilting and the rotation speed [1-3,6].

Another approach to modify the film microstructure, as compared to what is obtained in conventional deposition conditions, is to replace argon by another sputtering gas. The effect of the sputtering gas on the sputtering mechanism and on the microstructure of thin films has been studied in the recent years [7-9]. Helium may be a good candidate because its behavior in many materials has been studied for 20 years in the frame of fusion reaction [10,11]. From research on implantation in various materials, it is well known that He, having low affinity with most

elements, tends to diffuse, aggregate and form defects called He-vacancy complexes that can grow in size until bubbles are formed [12]. In specific experimental conditions, when these mechanisms take place just below the surface, this can lead to the release of He, bubble emptying, flaking, and to the formation of a fuzz structure. Such porous nanostructures were observed on various metals such as tungsten [13-15], molybdenum, nickel, titanium, iron, aluminum [16-19], precious metals [20] and metallic alloys [21].

In order to take advantage of this specific behaviour of helium, magnetron sputtering has been studied in Ar/He gas mixtures or in pure He atmosphere [22-25]. Depending on the material and process parameters, it has been shown that performing magnetron sputtering in He results in the formation of open/closed porosity, namely nano-sized empty or He filled bubbles [23,26] and/or nanostructured porous thin films [27]. Lacroix et al. obtained cobalt coatings by magnetron sputtering using He gas, where large amounts of He were trapped inside the closed spherical and faceted nano-pores [23]. For several years, the same group has widely studied the deposition of thin silicon films by RF magnetron sputtering in pure helium [22,26,28]. Nano-pores filled with He oriented towards the growth direction have been evidenced. They showed that these He/Si layers exhibit interesting properties and may serve as solid He targets for nuclear reactions [26], or be used in the design of Bragg reflectors [28]. In another study, Iyyakkunnel et al. reported the formation of tungsten porous films, during RF magnetron sputtering using 92 % He in an Ar/He atmosphere, and pure He plasma [25]. Helium was detected inside the film by glow discharge optical emission spectroscopy and the stability of the He trapping was investigated using thermal desorption. The nanostructures obtained were attributed to the impact of helium on the film growth process, hindering coarsening and forcing renucleation. Recently we investigated the deposition of Al thin films in various Ar/He mixtures in order to gain better insight into the modification of the sputtering process at the target and the deposition conditions at the substrate when He is present in the gas phase [27]. We

evidenced that when the sputtering plasma starts to be dominated by He ions, both sputtering and deposition processes are greatly affected.

Even if some trends have been identified, not all the complex mechanisms taking place at the substrate during the film growth in He are yet fully understood. In order to contribute to the understanding of these mechanisms we decided to investigate the growth of Al and Si in pure He and similar deposition conditions. The microstructural properties of the films have been investigated by scanning electron microscopy (SEM), transmission electron microscopy (TEM) and X-ray diffraction (XRD) techniques. Both Rutherford backscattering spectrometry (RBS) and proton elastic backscattering spectrometry (PEBS) were conducted to determine the number of Al(Si) and He atoms in the films, respectively. Moreover, insights that Doppler broadening positron annihilation spectroscopy (DB-PAS) analysis could bring to the characterization of helium-related defects in aluminum and silicon films were explored. When DB-PAS is coupled to a slow positron beam it is possible to probe a thin layer at the first micron under the surface of He implanted materials [29,30]. It has been successfully used to characterize Ti films deposited in various Ar/He mixtures [31]. In addition, PAS can be a suitable probe to identify open porosity, manifested by positronium (Ps; an electron-positron atom-like bound state) escape in vacuum. To study the sputtering process of Al and Si targets by He ions and to predict energy distribution functions (EDF) of sputtered Al(Si) and backscattered He atoms leaving the target and arriving at the substrate, SRIM software [32] and a homemade code were employed [33].

2. Experiments and models

2.1. Deposition Experiments

Al and Si nanostructured films were grown by direct current (DC) magnetron sputtering using pure helium as a deposition gas. The films were deposited onto (100) oriented N-type Si wafers by sputtering a 4-inch Al target and a 2-inch Si target (99.999% purity from Neyco) in different plasma reactors and similar deposition conditions. A complete description of the setups for Al and Si deposition can be found in references [27] and [26], respectively. Basically, the Al film was deposited in DC mode during 1 hour at a constant current of 1.2 A and a pure He pressure of 4.2 Pa [27]. The input power was about 350 W (surface power density of 4.3 W/cm^2) for a cathode voltage of 290 V. The substrates were maintained on a rotating substrate holder, and the distance between the substrate and the target was fixed to 12 cm [27]. The deposition of Si film was performed during 4 hours at a constant power of 100 W in DC mode (surface power density of 5 W/cm^2), a current of 0.25 A (370 V cathode voltage) and a pure He pressure of 4.8 Pa. In this case, the distance between the substrate and the target was 10 cm.

2.2. Characterization methods of thin film morphological and structural properties

SEM, TEM and high-resolution transmission electron microscopy (HRTEM) analyses were performed using two FEG-SEM (a Carl Zeiss supra-40 FEG-SEM and a HITACHI S-4800 FEG-SEM operated at 1-2 kV); a Jeol 2100Plus TEM operated at 200 kV and an ARM CFEG JEOL TEM working at 200 kV and equipped with 2 Cs aberration correctors. For cross section observations a conventional preparation protocol was used. First, the sample is cut into thin slices with thickness of the order of 1 mm. A sandwich structure is prepared by bonding two slices, prepared with the deposited layers facing each other. The structure is then cut into slices mounted on a tripod and the specimen is mechanically polishing. At the end, this specimen is glued to a 3 mm diameter copper support and a broad argon ion beam system is used to polish

the specimen so that the thinnest portions of the wedge are at the center for HRTEM imaging and analytical techniques. Electron energy loss spectrometry (EELS) was performed on the Carl Zeiss HRTEM. Gatan imaging filter (GIF) Quantum ER 965 equipped with dual a EELS option was used to acquire the zero loss peak (ZLP) and low loss spectrum area with different acquisition times, in order to increase the signal-to-noise ratio. The spectrum resolution was measured as the full width at half maximum of the ZLP to be 0.46 eV. The used HRTEM and GIF parameters used such as the convergence angle and the collection angle were respectively 22.5 mrad 0.025 eV/Ch. The crystal structure of both films was characterized using a Bruker D8 Discover X-ray diffractometer in the grazing incidence geometry (GIXRD) (Cu Kα radiation 1.5418 Å, 40 kV, 40 mA). The angle of incidence was set at 1°.

2.3. Ion beam and positron annihilation analyses

The ion beam analysis experiments were carried out at the Pelletron accelerator of CEMHTI laboratory (Orleans), a facility that is part of the EMIR&A French network of accelerators (http://emir.in2p3.fr).

The number of deposited Al(Si) atoms was determined by RBS using 2 MeV alpha particles with a 166° scattering angle and a 90 mm distance. The amount of He in the films was investigated by PEBS using 2.4 MeV protons and a 62 mm^2 passivated implanted planar silicon (PIPS) annular detector located at 178° scattering angle and 104 mm distance. The experimental spectra were simulated using the SIMNRA software [34] with the $^4He(p,p)^4He$ differential cross-sections measured by Langley [35]. The proportion of He incorporated inside the films was determined as the ratio of the areal atomic density of He atoms to that of Al(Si) atoms.

For DB-PAS implemented at the CEMHTI laboratory [36], a monoenergetic positron beam produced by a sodium Na-22 source was directed onto the sample and accelerated with adjustable energy ranging from 0.5 to 25 keV. For this energy range, the slow positrons probe

a thickness of roughly 3±2 μm in Al and Si films [37]. The positron-electron pair momentum distribution is measured at 300 K by recording the Doppler broadening of the 511 keV annihilation line with a Ge detector. Two shape parameters were extracted from the spectrum. The low momentum parameter S is the fraction of annihilations taking place with valence electrons. The high-momentum parameter W in the windows at the wings corresponds to the fraction of annihilations taking place with core electrons. It is important to note that each annihilation state (i.e. defect, bulk, surface…) is characterized with specific S and W values and when a material contains vacancy defects S increases and W decreases. The positronium fraction (Ps) can also be used as proof of the presence of defects in the sample. In the case of dense metals, Ps is formed with backscattered or reemitted positrons from the surface with a free electron. It is furthered when positrons are not efficiently trapped inside the sample and are thus able to diffuse back to the surface. Ps is also promoted when the accessible surface is wide, for instance in the presence of large empty pores or open porosity [38]. The positronium fraction measured in our sample was estimated using the method given by Schultz and Lynn [39].

2.4. Deposition conditions

Stopping and range of ions in matter (SRIM) software [32] was employed to investigate the interaction of the He ions accelerated in the cathode sheath with the Al(Si) target. It was possible to determine the sputtering yield, the backscattering yield of He ions and the energy distribution functions of particles emitted at the target under bombardment with 370 and 290 eV He ions in the case of Si and Al targets, respectively. These energy values correspond to ions that have not encountered collisions through the accelerating sheath between the plasma and the biased target. Since the working pressure is quite high (5Pa) several collisions may take place. Thus, one has to keep in mind that maximum values will be obtained by the estimations. Nevertheless, orders of magnitude will be valid as well as the comparison between Al and Si case.

Starting from these data, a simple collisional model of particle slowing down along straight-line trajectories and subjected to a continuous energy loss process by elastic collisions with the gas atoms was implemented [33]. The mean kinetic energy of sputtered atoms and backscattered He is calculated according to a modification of the Thompson formula, as the particles are travelling through a gaseous medium [40]. To calculate the energy loss (E_f) of sputtered atoms/backscattered He by collision with the gas atoms, a Maxwell–Boltzmann (MB) distribution at T_g is fixed for the gas (in our conditions T_g = 300 K, $E_g = k_B T_g$). Because we search for the complete energy distribution of sputtered atoms or backscattered He, for each E_g in the MB gas distribution, the energy loss is calculated for a fixed value of the kinetic energy E of a sputtered atom/backscattered He. This is repeated for each E in the Thompson distribution and weighted by the collision probability, which is simply the convolution of f(E) and the MB distribution at Tg [40]. More details can be found in reference 33. These calculations made it possible to determine the energy distribution functions (EDFs) (and thus the mean kinetic energy) of the particles at the substrate location after propagation in pure helium gas for a pressure and a target-substrate distance values identical to the experimental conditions.

3. Results

3.1. Al and Si thin film characteristics

Figure 1 shows the GIXRD patterns of Al film. It presents the face-centered-cubic (fcc) crystal structure, where the peaks corresponding to (111), (200), (220), (311), and (222) crystallographic planes are identified. The intensity of the peaks is similar to those given in the ICCD file (PDF card -00-004-0787) indicating that the Al film is polycrystalline and randomly oriented. Moreover, the peak positions are not shifted indicating that no residual stress is present

in the film. On the contrary, no peaks were detected on the diffractogram of the Si sputtered thin film (not given) which highlights the presence of an amorphous structure.

Figure 2 presents the cross-section and top-view SEM images of the Al and Si films. Completely different morphologies are shown. Above a 150 nm dense zone, the Al film is highly porous, formed of fiberform nanostructures on which nanoparticles are visible. On the contrary, the Si film appears quite dense, but some pores of about 50 nm are observed at the surface and on the magnified image of the cross section (figure 2b).

In order to investigate the insertion of He inside the films, PEBS spectra are presented in figure 3. Qualitatively it is seen that the amount of captured He is much higher in Si. From the number of He atoms (at/cm^2) obtained by PEBD and the Al(Si) ones obtained by RBS, the atomic percent of He inserted inside the film can be calculated. We found 5% for Al and 45% for Si, respectively. This very high value obtained for Si is in accordance with previous and recent studies on Si films elaborated by magnetron sputtering [22, 41-42].

To gain further insight into the film structure and the insertion of He, HRTEM analyses were performed. For the Al film, images 4a and 4b are in good agreement with SEM results: the film is composed of a first dense layer topped with a porous part made of fiberform nanostructures over about 1 µm depth. On the underfocused and overfocused images 4c and 4d, the complexity of the structure is visible and pores of various sizes are evidenced (red arrow). EELS was carried out to try to detect He at this small scale, and determine whether pores are empty or filled with He. A He peak corresponding to its ionization energy is expected at about 22 eV, it is presented in figure 4. The other peak visible on the EELS spectra is well known [43]. It corresponds to electrons that have induced the excitation of two Al plasmons (peak located at 15 eV, not shown on the figure). It appears at an energy twice of that of the plasmon, i.e. 30 eV. EELS analysis shows that most of the bubbles in the dense part contain He, some of them being faceted. All

the observations made on this sample indicate that the porous part of the layer contains fewer pores, which are not always filled with He.

Cross section TEM images of the Si film are presented in figure 5 at three magnifications. On figure 5a a first more dense layer (about 150 nm thick) is visible at the interface with the substrate, as on the Al film. It has a different contrast than the columnar dense structure observed above. At high magnification, it can be seen that these columns are formed of elongated pores (or bubbles) with the smallest dimension mainly below 10 nm. Nevertheless, several of them reach 20 nm. These patterns are oriented in the film growth direction. In their recent work on magnetron sputtered Si films, Fernandez et al evidenced the same kinds of microstructures, when either an RF or a DC supply was used [44]. By EELS analysis they also demonstrated that, in the case of films deposited by RF magnetron sputtering, these pores are He bubbles in which the corresponding He pressure may reach values as high as 1 GPa [41]. These results also correlate with the high amount of trapped He detected by PEBS in the Si films (see Fig. 3).

PAS was conducted on both films in an attempt to detect defects, pores or He bubbles. One has to keep in mind that this technique is well suited to detect, and in some favorable conditions to quantify, vacancy defects of different natures. Several studies have reported the signature of He-filled pores, in tungsten [29,45,46] and silicon based materials [37,47]. On figure 6 are plotted both the S parameter and the positronium fraction as a function of the positron energy for Al and Si films and a reference of each material: silicon substrate for Si and Al film deposited in Ar (4 µm thick, dense columnar structure) for Al. In all samples, the W parameters (not shown here) as a function of the positron energy behave inversely to the S parameter. It is important to note that the depth analysis in DB-PAS depends on the density of the materials. In dense silicon and aluminum, the mean implantation depth is about 10 nm at 1 keV in both materials, and 1.25 µm and 1.05 µm at 15 keV and 3 µm and 2.5 µm at 25 keV, respectively.

First, in the two reference samples, the S parameter evolves rapidly from the surface value to reach a plateau at 4 keV indicating that above 100 nm positrons probe homogeneous layers. The positronium fractions show the same trend for both references and decrease rapidly to reach negligible values above 4 keV. At 0.5 keV, the estimated Ps fraction is 5.7% in the reference Al sample. This could be related to a high level of vacancy defects with large open volumes present in the sample since the Al film deposited in Ar exhibits a columnar structure with a non-negligible porosity.

Concerning the Al film obtained in pure He, the evolutions of both the S parameter and Ps evidence a domain between 1 keV and 12 keV where values are different from those of the Al reference. The high S values obtained in this part of the sample (below 800 nm) highlight the presence of a higher concentration of vacancy defects or larger defects than in the reference layer. Furthermore, the high positronium fraction confirms the presence of large empty pores in the film that exhibit an extended surface where numerous Ps can be formed. These observations are in accordance with SEM, TEM and PEBS results, i.e. formation of an Al film containing vacancy defects whose nature (He-filled or empty) and size evolve along the thickness, exhibiting high open porosity.

The S parameter evolves differently in the Si film compared to the Al film. Very high values are measured close to the surface and a linear decrease is observed over several microns down to the substrate value. An inhomogeneous defect concentration is detected by positrons over this layer, which suggests the presence of large defects, or a concentration of pore near the surface. On the other hand, the Ps fraction remains low in this sample, indicating that almost no empty, nor open pores, are detected by positrons. The reason could be that the presence of He in vacancies or pores can prevent the formation of positronium [38] or the trapping of positrons, and thus impede their detection. This is in accordance with PEBS and EELS results, which show that 45% of He is still present in this layer. Thus the observed S parameter and Ps

fraction behaviour can be explained by the presence of He filled defects but indicates that a non-negligible proportion of the pores detected by TEM are empty.

3.2. Sputtering process and gas phase features

Replacing the Ar gas conventionally used in magnetron sputter deposition by He has two main consequences at the target related to the low mass of helium. First, the sputtering rate is decreased as shown in table I and as reported in the literature. Second, the probability for the bombarding ions to be backscattered towards the substrate rises. During this process, the positive ions are neutralized at the target and become fast neutrals that assist the film growth [27].

Table 1 shows that the SRIM sputtering yield of Al by He ions is almost twice as high as that of Si, in the present experimental conditions (the energy gained through the plasma potential is neglected and only the cathode voltages of 290 and 370 V are taken into account). This is the reason why the deposition times have to be adapted to deposit films of equivalent thicknesses. Besides, SRIM calculations reveal that almost 20% of He ions are backscattered in both cases. From these yield values and taking into account the angular distributions of Al(Si) versus He (given by SRIM), we roughly evaluated that the number of fast He atom impinging the substrate when one Al(Si) atom condenses at the surface (fast He atom / Al(Si) atom ratio) is of 1/7 for Al, whereas it reaches 1/3 in the case of Si.

Figure 7 presents the EDF of sputtered Al(Si) atoms and fast He neutrals at the target and the substrate positions. Table 2 shows the values of the mean kinetic energy for each species calculated from the EDFs. Thanks to the similar deposition conditions used for Al and Si films, the product P*d, which is known to be an important parameter to qualify the growth conditions

[48-50], is equivalent (50 Pa.cm and 48 Pa.cm respectively). Moreover, Al and Si have similar masses, thus the energies transferred during one collision with He atoms are similar.

It is seen on figure 7a that ejected Al and Si atoms exhibit quite similar EDF, reaching values as high as 80 eV. A closer look at the low energy part indicates that the EDF maximum is lower for Al than for Si, in accordance with the binding energy (E_b) of each element: 3.39 eV for Al and 4.63 eV for Si, respectively. EDFs of sputtered atoms have been widely studied and are well described by the collision cascade models used in the SRIM code. The maximum of the distribution depends only on E_b, and thus, on the nature of the sputtered element [51]. However, the evolution of the energy distribution at higher energies is related to the mass difference between the ion and the sputtered element, and to the ion kinetic energy [52]. Since the two parameters are very close in our experiments for Al and Si, this part of the EDFs at the target position is similar. Globally the mean kinetic energies of sputtered Al atoms and Si atoms at the target given in table 2 (E_{Al} = 24 eV and E_{Si} = 20 eV) are not significantly different. Figure 7 (c) shows the EDF of fast He neutrals at the target as calculated by SRIM. In both cases, a broad EDF is obtained showing that He atoms with kinetic energies of several hundreds of eV leave the target. The maximum predicted value is higher in the case of Si, since the accelerating cathode voltage was higher in the Si (370 eV) than in the Al (290 eV) experiments.

To investigate the film growth, it is necessary to know the EDFs at the substrate. They were evaluated using simple calculations of energy loss by collisions with the gas atoms [33]. As mentioned above, the P*d product and element mass are similar in both experiments, which could ensure similar conditions of transport in the gas phase. However on Figure 7 (b) it is seen that the EDFs of the sputtered Al and Si atoms at the substrate position are quite different. This is due to the difference of scattering cross sections linked to the atomic radii of the elements: 1.82 Å for Al and 1.46 Å for Al and Si, respectively. Thus, even if the energy transfer efficiency is similar, the probability of He/atom collision is larger for Al. The cooling effect due to

collisions with He is much more effective for Al atoms than for Si ones as shown on figure 7 (b). However, the mean kinetic energies for Al and Si atoms at the substrate given in table 2 are not so different: 0.1 eV and 0.2 eV, respectively. The same comment can be made for the fast He atoms for which 8 and 10 eV are obtained at the substrate location for Al and Si respectively.

4. Discussion

By correlating the film analysis carried out in this study, knowledge from He implantation studies and data extracted from the SRIM/transport codes, it is possible to gain some insights into the main parameters driving the formation of Al and Si films in He.

The mean kinetic energies of Al and Si atoms condensing at the substrate in the present work (4 Pa of He) lie below 1 eV, which is quite low for magnetron sputtering deposition [53] conventionally operating at 0.5 to 1 Pa in Ar. However, energetic He species, formed by backscattering and neutralization of He ions at the target, carry energies around 10 eV and assist the film growth. The proportion of backscattered He ions on Al and Si targets is high, close to the sputtering yield (see table 1), indicating that this specie has to be taken into account. This is confirmed by the study of Gauter et al. on energy transfers during magnetron sputter deposition of various elements carried out in three gases [54]. They found out that the energetic contribution due to backscattered gas atoms play an important role when He is used. Moreover, because of the high thermal conductivity of He [55], and of the high pressure, thermal transfer from the target, heated by the sputtering process, to the reactor surfaces occurs. This is highlighted by the temperature rise of the external walls during the growth that lasts between 1 to 4 hours. All this suggests that energy is transferred from the target to the substrate during the growth (fast He species and thermally heated gas atoms) and that the surface mobility of the adatoms is certainly furthered as compared to the Ar case.

In a previous study we proved that insertion of He in an Al thin film is related to the presence of backscattered/neutralized He ions becoming fast neutrals. This suggests that, even if conditions are different (He^+ flux and kinetic energy, substrate temperature etc.), a comparison between the mechanisms of He insertion during implantation experiments and He insertion during magnetron sputter deposition may be fruitful. In their work on Ti thin film deposition, Liu et al. suggested that "a continuous sub-threshold-energy implantation process" occurs [24].

As mentioned in the introduction, the implantation of He and its behavior inside the lattice have been widely studied in many materials. In their work on metal surface modification by He implantation Tanyeli et al. found that the formation of nanostructures/porosity is promoted by adatom creation and diffusion, sputtering, and a mechanism specific to He, namely void formation via the emptying of gas filled bubbles [17]. This process can only occur when He accumulates and is trapped in bubbles very close to the surface meaning at "low" kinetic energies, typically below 50 eV. In a previous study of He^+ implantation in W, we showed that a decrease in the ion kinetic energy promotes the accumulation of He in large bubbles just below the surface that tend to easily break, releasing He, which induces the formation of open porosity [46]. This is furthered in the present work, where the kinetic energy of the He ions is estimated between 5 to 20 eV. After the implantation step, He mobility inside the lattice is required for the formation of gas bubbles via a complex and well-described mechanism. He diffuses easily in the lattice, forming interstitial clusters that are mobile and act as trapping sites for the further in-coming He atoms. Above a certain size, He clusters are able to push out lattice atoms and create He-vacancies which are bubble seeds [12,56,57]. At the atomic scale, these elementary processes (atom/cluster diffusion, vacancy formation) involve lattice atoms and thus depend on the crystallographic phase and degree of crystallinity of the material. In our deposition conditions Si films are amorphous, whereas polycrystalline coatings are obtained for Al. Moreover, Al crystallizes in FCC phase, which has been found favorable to He diffusion and

the clustering process. This was pointed out by Tanyeli who reported the growth of nano-pillars on an Al surface submitted to bombardment by 25-35 eV He ions [17].

Tanyeli pointed out that nanobubble formation near the surface is necessary but not sufficient to give rise to nanostructure formation [17]. The presence of mobile adatoms able to diffuse at the surface is also required. This is confirmed by Kajita et al. who investigated the growth of nanofibers on Re and Ru surfaces submitted to He plasma. They highlighted that the conventional growth model based on stress induced inside the metal by He bubbles that pushes up the fiberform structures cannot explain all their observations. They suggested a growth process based on the diffusion of adatom formed by He sputtering along the nanofiber [58]. In magnetron deposition technique adatoms are, of course, present at the surface and no particular mechanism of creation (sputtering, pushing up by He bubbles…) has to be invoked.

The question is: is the mobility at the surface high enough to sustain the growth of fiberform nanostructures? Surface mobility can be defined, in terms of the T/T_m ratio for metals. For example Kajita et al. reported that the nanostructuration of W takes place at temperatures in the range $0.25 \langle T/T_m \langle 0.55$ [59]. Measuring temperature is an extremely complex issue and is always highly questionable. However, values that we obtained at the back of the substrate holder during metal sputtering in our experiments are about 80°C. We can reasonably assume that the corresponding domain may be reached for Al (160-360°C for a melting temperature of 660°C). On the contrary, because of its higher melting temperature (1410°C), significant enhancement of adatom mobility is more difficult to reach at the Si surface. In comparison and for similar deposition conditions, surface diffusion, and reorganization will be promoted in the case of Al.

Thus, it appears that, for Al, in our experiment, the appropriate conditions are met to produce nanostructures: fast He neutrals are implanted below the surface of the growing film, diffuse

easily, accumulate in mobile clusters then in bubbles that break, leading to the formation of open porosity. As the surface mobility is high, adatoms diffuse easily and nanostructures are able to grow. This is in accordance with the film properties highlighted: the signature of the formation of He bubbles and of He implantation is observed via DB-PAS, TEM (detection of voids and nano-pores) and PEBS, EELS (detection of a small amount of He). The presence of a dense 150 nm thick layer at the interface with the Si may be due to the fact that the formation of a first Al layer, is required for He to be implanted and, thus, for the nanostructure to be formed.

In the case of Si, the number of fast He atoms arriving at the substrate per condensing atom was estimated to be higher than for Al. As explained above, the energetic conditions at the substrate, for this high melting point element, do not allow significant surface mobility. Moreover, a very important parameter is the amorphous nature of the growing Si film. In a recent study, Liu et al. investigated He^+ implantation in crystalline and amorphous TiAl films deposited by magnetron sputter deposition [60]. They observed the formation of blisters in the first case, whereas in the amorphous film a swelling phenomenon is visible due to the stable insertion of He in bubbles. This was attributed to a lower He atom mobility in the anisotropic amorphous phase. Similar observations have been made for amorphous Si in investigations focusing on the irradiation of crystalline Si by keV He+. It was found out that nanopores are only formed in the zone where ion damage causes amorphization of the material [61]. This behavior was again attributed to a lower mobility of implanted He than in the crystalline part. Moreover, these pores are found aligned with the direction of ion motion throughout the radiation-induced amorphous zone. This result is in good agreement with ours, since He nano-bubbles in Si are clearly oriented toward the growth/implanted He atom direction.

5. Conclusions

In this work deposition of Al and Si films by DC magnetron sputtering was performed in He in similar conditions (power density at the target and distance x pressure product). Highly porous, polycrystalline films composed of fiberform nanostructures were obtained for Al in which no more than 5 at. % of He was detected. Amorphous columnar films were formed with Si containing 45 at. %. of He captured in nano-sized bubbles. Using SRIM and a homemade code, the sputtering of Al / Si targets and transport of the emitted particles were simulated to characterize the deposition conditions.

The results were compared to the literature on the modification of surface materials by low energy He ion implantation. Even if conditions at the substrate surface during magnetron sputtering deposition can not be directly compared to implantation experiments (higher ion flux, substrate temperature), the observations that we have made indicate that similar mechanisms take place. It is obvious from our results, and those from other authors, that He is inserted during the growth in the already deposited depth. The features of the films obtained (fiberform nanostructures and oriented bubbles) are very similar to those of He implanted surfaces. This leads us to think that fast He atoms formed by ion backscattering at the target play a role in the insertion process despite the high pressure and the high number of collisions between the target and the growing film. After this first step, depending on the element, different processes occur. In Al, where He-atom / He-cluster diffusion is promoted and global surface mobility is high, He release at the surface takes place and a porous structure made of fiberform nanostructures is formed. In the case of Si, as the mechanism of He diffusion is unlikely in an amorphous structure, He accumulates in stable nano-bubbles where it is efficiently trapped, and a gas/solid nanocomposite is formed.

Comparing elements of close masses in similar deposition conditions has permitted to highlight how the intrinsic features of the element (binding energy, crystalline structure) and the behavior

of He inside the lattice impact the film structure. This work contributes to the understanding of magnetron sputtering deposition basics and will pave the way for future design of nanoporous films of various kinds. Of course, since using He as the sputtering gas will increase the operating cost, applications will be restricted to high added value products or when not alternative solution exist.

Acknowledgements

This work was supported by the Centre Val de Loire region (APR-IA PRESERVE 2019-00134921 and the Fond Européen de Développement Régional EX010666). The authors thank LE STUDIUM Loire Valley Institute for Advanced studies, and Asunción Fernández also acknowledges the support by the Spanish and Junta de Andalucía grants nrs. RTI2018-093871-BI00, P20-00239 and PID2021-124439NB-I00 (all co-financed by EU FEDER). This project has benefited from the expertise and the facilities of the Platform MACLE - CVL which was co-funded by the European Union and Centre-Val de Loire Region (FEDER). We acknowledge the French EMIR&A network for provision of irradiation beam time and assistance in using the CEMHTI-Pelletron facility.

References

[1] J. Dervaux, P.-A. Cormier, P. Moskovkin, O. Douheret, S. Konstantinidis, R. Lazzaroni, S. Lucas, R. Snyders, Synthesis of nanostructured Ti thin films by combining glancing angle deposition and magnetron sputtering: A joint experimental and modeling study, Thin Solid Films. 636 (2017) 644–657.

[2] M.M. Hawkeye, M.T. Taschuk, M.J. Brett, Glancing angle deposition of thin films: engineering the nanoscale, John Wiley & Sons, 2014.

[3] A. Barranco, A. Borras, A. R. Gonzalez-Elipe, A. Palmero, Perspectives on oblique angle deposition of thin films: From fundamentals to devices, Progress in Materials Science. 76 (2016) 59–153.

[4] E. Greene, Review Article: Tracing the recorded history of thin-film sputter deposition: From the 1800s to 2017, J. Vac. Sci. Technol. A 35, 05C204 (2017).

[5] K. Sarakinos, J. Alami, S. Konstantinidis, High Power Pulsed magnetron Sputtering: a review on Scientific and Engineering State of the Art, Surface & Coatings Technology. 204 (2010) 1661-1684.

[6] A. Siad, A. Besnard, C. Nouveau, P. Jacquet, Critical angles in DC magnetron glad thin films, Vacuum. 131 (2016) 305–311.

[7] S. Zenkin, A. Gaydaychuk, S. Linnik, Effects of sputtering gas on the microstructure of Ir thin films deposited by HiPIMS and pulsed DC sputtering, Surface and Coatings Technology. 412 (2021)127038.

[8] S. Cuynet, T. Lecas, A. Caillard, P. Brault., An efficient way to evidence and to measure the metal ion fraction in high power impulse magnetron sputtering (HiPIMS) post-discharge with Pt, Au, Pd and mixed targets, Journal of Plasma Physics. 82(6) (2016) 695820601.

[9] S. Gauter, F. Haase, H. Kersten, Experimentally unraveling the energy flux originating from a DC magnetron sputtering source, Thin Solid Films. 669 (2019) 8-18.

[10] A.W. Kleyn, W. Koppers, N. Lopes Cardozo, Plasma-surface interaction in ITER, Vacuum. 80 (2006) 1098e1106.

[11] R.E. Nygren, R. Raffray, D. Whyte, M.A. Urickson, M. J. Baldwin, L.L. Snead, Making tungsten work - ICFRM-14 session T26 paper 501, J. Nucl. Mater. 417 (2011) 451-456.

[12] L. Pentecoste, P. Brault, A.-L. Thomann, P. Desgardin, T. Lecas, T. Belhabib, M.-F. Barthe, T. Sauvage, Low energy and low fluence helium implantations in tungsten: Molecular dynamics simulations and experiments, Journal of Nuclear Materials. 470 (2016) 44-54.

[13] M.J. Baldwin, R.P. Doerner, Helium induced nanoscopic morphology on tungsten under fusion relevant plasma conditions, Nucl. Fusion. 48 (2008) 35001..

[14] M. Tokitani, S. Kajita, S. Masuzaki, Y. Hirahata, N. Ohno, T. Tanabe, Exfoliation of the tungsten fibreform nanostructure by unipolar arcing in the LHD divertor plasma, Nucl. Fusion 51 (2011) 102001. http://dx.doi.org/10.1088/ 0029-5515/51/10/102001.

[15] S. Takamura, N. Ohno, D. Nishijima, S. Kajita, Formation of nanostructured tungsten with arborescent shape due to helium plasma irradiation, Plasma and Fusion Research. 1 (2006) 051–051.

[16] I. Tanyeli, L. Marot, M.C. van de Sanden, G. De Temmerman, Nanostructuring of iron surfaces by low-energy helium ions, ACS Applied Materials & Interfaces. 6 (2014) 3462–3468.

[17] I. Tanyeli, L. Marot, D. Mathys, M. C. M. van de Sanden, G. De Temmerman, Surface Modifications Induced by High Fluxes of Low Energy Helium Ions, SCIENTIFIC REPORTS. 5 (2015) 9779.

[18] S. Kajita, T. Yoshida, D. Kitaoka, R. Etoh, M. Yajima, N. Ohno, H. Yoshida, N. Yoshida, and Y. Terao, Helium plasma implantation on metals: Nanostructure formation and visible-light photocatalytic response, Journal of Applied Physics. 113 (2013) 134301.

[19] S. Takamura, Y. Uesugi, Experimental identification for physical mechanism of fiber-form nanostructure growth on metal surfaces with helium plasma irradiation, Applied Surface Science. 356 (2015) 888–897.

[20] S. Kajita, T. Nojimab, Y. Tomitab, N. Ohnob, H. Tanakab, N. Yoshidac, M. Yajimad, T. Akiyamad, M. Tokitanid, T. Yagi, Fuzzy nanostructure growth on precious metals by He plasma irradiation, Surface & Coatings Technology. 340 (2018) 86–92.

[21] L. Wang X.P. Wanga, L.F. Zhanga, Y.X. Gao, R. Liu, R. Gao, Y. Jiang, T. Hao, T. Zhang, Q.F. Fang, C.S. Liu, Helium desorption behavior and growth mechanism of helium bubbles in FeCrNi film, Nuclear Materials and Energy. 21 (2019) 100710.

[22] Godinho V, Caballero-Hernández J, Jamon D, Rojas T C, Schierholz R, García-López J, Ferrer F J and Fernández, A new bottom-up methodology to produce silicon layers with a closed porosity nanostructure and reduced refractive index, Nanotechnology. 24 (2013) 275604.

[23] B. Lacroix, V. Godinho, A. Fernández, The nanostructure of porous cobalt coatings deposited by magnetron sputtering in helium atmosphere, Micron. 108 (2018) 49–54.

[24] C.-Z. Liu, L. Shi, Z. Zhou, X. Hao, B. Wang, S. Liu, L. Wang, Investigations of helium incorporated into a film deposited by magnetron sputtering, Journal of Physics D: Applied Physics. 40 (2007) 2150.

[25] S. Iyyakkunnel, L. Marot, B. Eren, R. Steiner, L. Moser, D. Mathys, M. Düggelin, P. Chapon, E. Meyer, Morphological changes of tungsten surfaces by low-flux helium plasma treatment and helium incorporation via magnetron sputtering, ACS Applied Materials & Interfaces. 6 (2014) 11609–11616.

[26] A. Fernández, D. Hufschmidt, J.L. Colaux, J.J. Valiente-Dobón, V. Godinho, M.C.J. de Haro, D. Feria, A. Gadea, S. Lucas, Low gas consumption fabrication of 3He solid targets for nuclear reactions, Materials & Design. 186 (2020) 108337.

[27] S. Ibrahim, F.Z. Lahboub, P. Brault, A. Petit, A. Caillard, E. Millon, T. Sauvage, A. Fernández, A.-L. Thomann, Influence of helium incorporation on growth process and properties of aluminum thin films deposited by DC magnetron sputtering, Surface and Coatings Technology. 426 (2021) 127808.

[28] J. Caballero-Hernández, V. Godinho, B. Lacroix, M. C. Jiménez de Haro, D. Jamon, and A. Fernández, Fabrication of Optical Multilayer Devices from Porous Silicon Coatings with Closed Porosity by Magnetron Sputtering, Appl. Mater. Interfaces. 7 (2015), 13889−13897.

[29] P.E. Lhuillier, T. Belhabib, P. Desgardin, B. Courtois, T. Sauvage, M.F. Barthe, A.L. Thomann, P. Brault, Y. Tessier, Helium retention and early stages of helium-vacancy complexes formation in low energy helium-implanted tungsten, J. Nucl. Mater. 433 (2013).

[30] R. Krause-Rehberg, H.S. Leipner, Positron Annihilation in Semiconductors: Defect Studies, Springer Science & Business Media, 1999.

[31] Y. Li, A.-H. Deng, Y.-L Zhou., B. Zhou, K. Wang, Q. Hou, L.-Q Shi., X.-B Qin, B.-YWang, Helium-Related Defect Evolution in Titanium Films by Slow Positron Beam Analysis, Chin. Phys. Lett. Vol. 29, No. 4 (2012) 047801.

[32] J.F. Ziegler, M.D. Ziegler, J.P. Biersack, SRIM–The stopping and range of ions in matter (2010), Nuclear Instruments and Methods in Physic Research Sect. B Beam Interactions with Materials and Atoms 268 (2010) 1818–1823.

[33] L. Xie, P. Brault, J.-M. Bauchire, A.-L. Thomann, L. Bedra, Molecular dynamics simulations of clusters and thin film growth in the context of plasma sputtering deposition, Journal of Physics D: Applied Physic 47 (2014) 224004.

[34] M. Mayer, Improved physics in SIMNRA 7, Nuclear Instruments and Methods in Physics Research Section B: Beam Interactions with Materials and Atoms. 332 (2014) 176–180. https://doi.org/10.1016/j.nimb.2014.02.056.

[35] R.A. Langley, Proc. Int. Conf. on Radiation Effect and Tritium Technology for Fusion Reactors, vol IV, J.S. Walson and F.W. Wiffen eds. (1976) 158.

[36] P. Desgardin, L. Liszkay, M.-F. Barthe, L. Henry, J. Briaud, M. Saillard, L. Lepolotec, C. Corbel, G. Blondiaux, A. Colder, P. Marie, M. Levalois, Slow positron beam facility in Orleans, Mater. Sci. Forum 363e365 (2001) 523e525.

[37] F. Linez, E.Gilabert, A.Debelle, P.Desgardin, M.-F.Barthe, Helium interaction with vacancy-type defects created in silicon carbide single crystal, Journal of Nuclear Materials. 436 (2013) 150–157

[38] M. P. Petkov, C. L. Wang, M. H. Weber, K. G. Lynn, K. P. Rodbel, Positron annihilation techniques suited for porosity characterization for thin film, Journal of Physical Chemistry B 107 (2003) 2725-2734.

[39] P. J. Schultz and K. G. Lynn, Interaction of positron beams with surfaces, thin films, and interfaces, Reviews of Modern Physics 60 (1988), 701.

[40] Meyer K, Schuller I K and Falco C M 1981 Thermalization of sputtered atoms J. Appl. Phys. 52 5803–5.

[41] R. Schierholz, B. Lacroix, V. Godinho, J. C.-Hernández, M. Duchamp3 and A. Fernández, STEM–EELS analysis reveals stable high-density He in nanopores of amorphous silicon coatings deposited by magnetron sputtering, Nanotechnology. 26 (2015) 075703 (10pp).

[42] V. Godinho, F. J. Ferrer, B. Fernández, J. Caballero-Hernández, J. Gómez-Camacho, A. Fernández, Characterization and Validation of a-Si Magnetron-Sputtered Thin Films as Solid He Targets with High Stability for Nuclear Reactions, ACS Omega. 1 (2016) 1229−1238.

[43] T. Stöckli, P. Stadelmann and A. Châtelain, Low-Loss EELS Study of Oxide-Covered Aluminum Nanospheres, Microsc. Microanal. Microstruct. 8 (1997), 145-155.

[44] A. Fernández, T. Sauvage, B. Diallo, D. Hufschmidt, M.C. Jiménez de Haro, O. Montes, J.M. Martínez-Blanes, J. Caballero, V. Godinho, F.J. Ferrer, S. Ibrahim, P. Brault, A.-L. Thomann, Microstructural characterization and thermal stability of He charged amorphous silicon films prepared by magnetron sputtering in helium, Materials Chemistry and Physics 301 (2023) 127674.

[45] V. Sabelova, V. Krsjak, J. Kuriplach, Y. Dai, V. Slugen, Coincidence Doppler broadening study of Eurofer 97 irradiated in spallation environment, J. Nucl. Mater. 458 (2015) 350e354.

[46] L. Pentecoste , A.-L. Thomann, P. Brault, T. Lecas , P. Desgardin, T. Sauvage, M.-F. Barthe, Substrate temperature and ion kinetic energy effects on first steps of He implantation in tungsten: Experiments and simulations, Acta Materialia. 141 (2017) 47-58

[47] B. Li, V. Krsjak, J. Degmova, Z. Wang, T. Shen, H. Li, S. Sojak, V. Slugen, A. Kawasuso, Positron annihilation spectroscopy study of vacancy-type defects in He implanted polycrystalline α-SiC, Journal of Nuclear Materials. 535 (2020) 152180.

[48] A.-L. Thomann, A. Caillard, M. Raza, M. El Mokh, P.A. Cormier, S. Konstantinidis, Energy flux measurements during magnetron sputter deposition processes, Surface & Coatings Technology. 377 (2019) 124887.

[49] S. Mraz and Jochen M. Schneider, Structure evolution of magnetron sputtered TiO2 thin films, Journal of Applied Physics. 109, 023512-2011.

[50] T.P. Drüsedau, M. Lohmann, F. Klabunde, T.-M. John, Investigations on energy fluxes in magnetron sputter-deposition: implications for texturing and nanoporosity of metals, Surface and Coatings Technology. 133-134 (2000) 126-130.

[51] Y. Yamamura, H Tawara, Energy dependence of ion-induced sputtering yields from monoatomic solids at normal incidence, Atomic Data and Nuclear Data Tables. 62 (1996) 149-253.

[52] K. Meyer, I. K. Schuller and C. M. Falco, Thermalization of sputtered atoms, Journal of Applied Physics. 52 (1981) 5803.

[53] H. Kersten, H. Deutsch, H. Steffen, G.M.W. Kroesen, R. Hippler, The energy balance at substrate surfaces during plasma processing, Vacuum. 63 (2001) 385–431.

[54] S. Gauter, F. Haase, H. Kersten, Experimentally unraveling the energy flux originating from a DC magnetron sputtering source, Thin Solid Films 669 (2019) 8–18

[55] Normand C. Blais, Joseph B. Mann, Thermal conductivity of helium and hydrogen at high temperatures, Journal of Chemical Physics. 32 (1960) 1459.

[56] L. Hu, K.D. Hammond, B.D. Wirth, D. Maroudas, Dynamics of small mobile helium clusters near tungsten surfaces, Surface Science. 626 (2014) L21.

[57] L. Hu, K.D. Hammond, B.D. Wirth, D. Maroudas, Molecular-dynamics analysis of mobile helium cluster reactions near surfaces of plasma-exposed tungsten, Journal of Applied Physics. 118 (2015) 163301.

[58] Shin Kajita, Tomohiro Nojima, Tatsuki Okuyama, Yuta Yamamoto, Naoaki Yoshida, Noriyasu Ohno, elium-plasma–induced straight nanofiber growth on HCP metals, Acta Materialia. 181 (2019) 342–351.

[59] Kajita, S., Sakaguchi, W., Ohno, N., Yoshida, N. & Saeki, T. Formation process of tungsten nanostructure by the exposure to helium plasma under fusion relevant plasma conditions, Nuclear Fusion. 49 (2009) 095005–6.

[60] Pei Liu, Lifeng Tian, Xuanze Li, Yutian Ma, Jing Xia, Xiangmin Men Structural evolution of amorphous and nanocrystalline TiAl films under helium implantation, Surface & Coatings Technology. 441 (2022) 128523)

[61] V. F. Reutov and A. S. Sokhatski, Formation of Ordered Helium Pores in Amorphous Silicon Subjected to Low-Energy Helium Ion Irradiation, Technical Physics, Vol. 48, No. 1, 2003, pp. 68–72. Translated from Zhurnal Tekhnichesko Ï Fiziki, Vol. 73, No. 1, 2003, pp. 73–78

Table I: sputtering yields and backscattering probabilities calculated from SRIM simulations of the interaction between He(Ar) ions (of 290 eV and 370 eV respectively) and aluminum or silicon amorphous targets.

	E_{ion} (eV)	**Sputtering yield in at/ion He/(Ar)**	**Backscattering probability (%) of He**
Al	290	0.22/(0.63)	19
Si	370	0.13/(0.36)	19.5

Table II: Mean kinetic energies of sputtered atoms and backscattered He atoms at the target and substrate as calculated from SRIM data [32] and a homemade code [33].

			$E_{\text{at the target}}$ (eV)		$E_{\text{at the substrate}}$ (eV)	
X: Al / Si	**P_{He} (Pa)**	**$d_{\text{substrate-target (cm)}}$**	**X**	**He**	**X**	**He**
Al	4.2	12	24	108	0.1	8
Si	4.8	10	20	140	0.2	11

Figure captions

Figure 1: GIXRD pattern of the Al thin film. Planes of the face centered cubic phase of Al are labelled.

Figure 2: Cross section (a and b) and top view (b and d) SEM images of Al (a and c) and Si (b and d) thin films.

Figure 3: PEBS spectra of Al (green) and Si (pink) thin films.

Figure 4: TEM observations and He bubbles identification in Al thin film. a) TEM BF image of cross section of the whole multilayer thin film; b) TEM Zero Loss filtered image of the base layer with 1µm underfocused (c) and overfocused images (d) showing bubbles (ref arrow). (e) STEM HAADF image of Al cross section and (f) magnification area of region of interest showing the spectrum image area acquisition for 4 extracted EELS Spectra (S1 to S4). g) EELS of 3 bubbles in base area of Al deposit showing He pics around 22 eV (S1 to S3), and EELS of Al outside the bubbles (S4).

Figure 5: TEM images of the cross section of the Si film at three magnifications.

Figure 6: S parameter (left) and positronium fraction (right) evolution with respect to the positron energy for Al film deposited in Ar, Si wafer (substrate) and Al, Si films deposited in He. The mean positron implantation depth in nm is given for silicon.

Figure 7: EDFs of sputtered Al, Si atoms and backscattered He atoms obtained from SRIM and an homemade code at the target (a and c) and the substrate (b and d) locations.

Figures

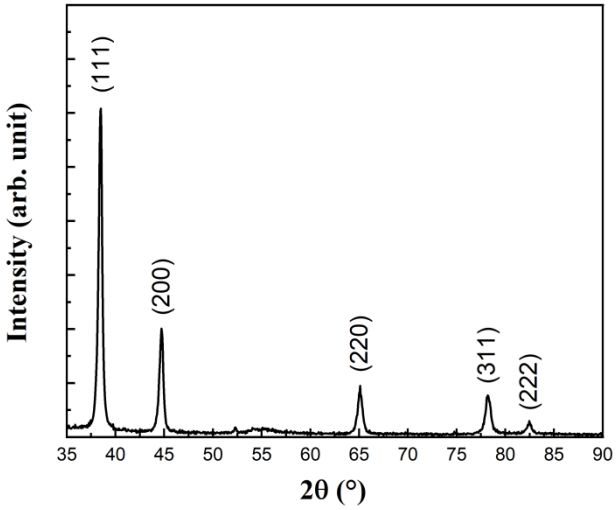

Figure 1

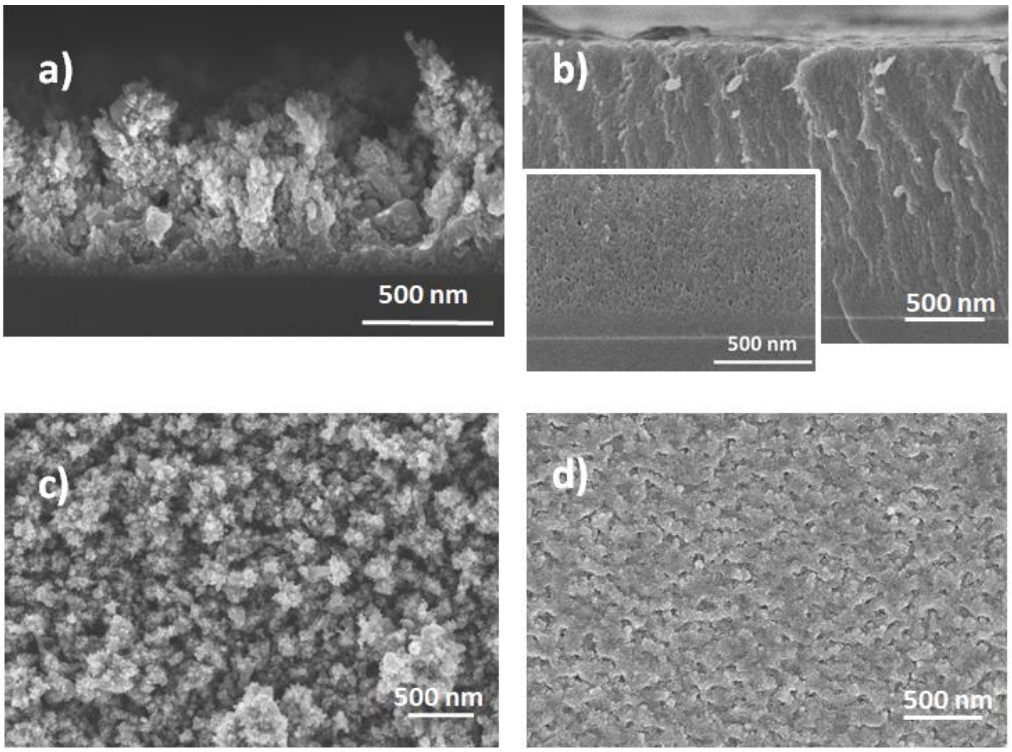

Figure 2

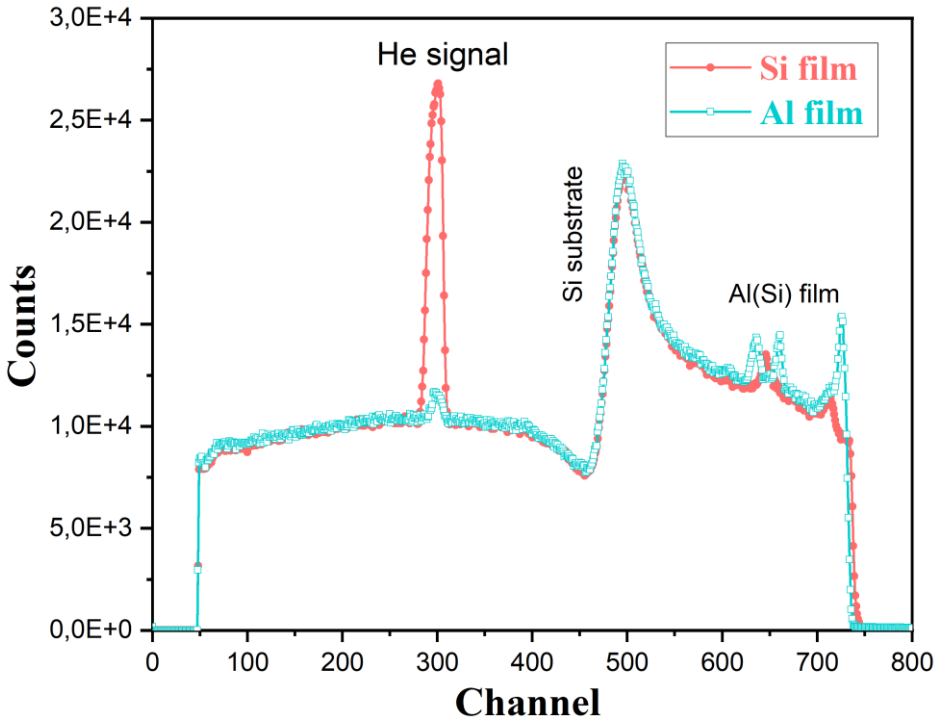
He signal
Si film
Al film
Si substrate
Al(Si) film
Counts
Channel
3,0E+4
2,5E+4
2,0E+4
1,5E+4
1,0E+4
5,0E+3
0,0E+0
0
100
200
300
400
500
600
700
800

Figure 3

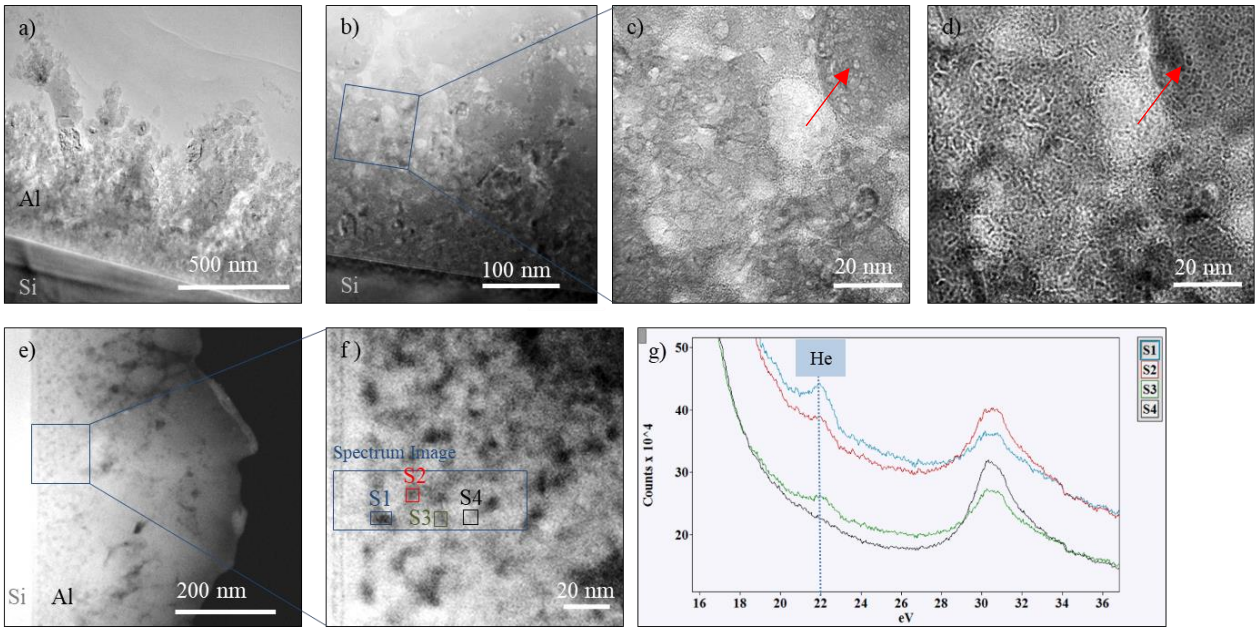

Figure 4

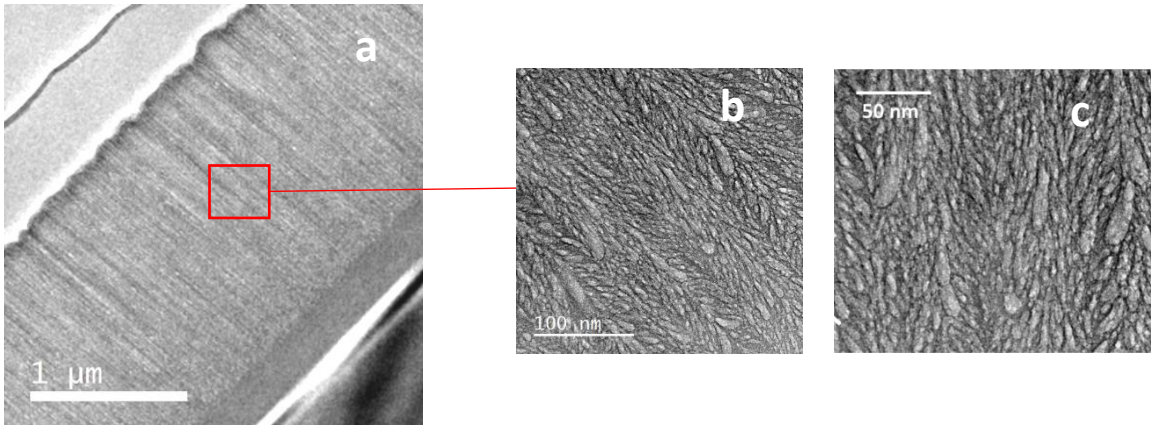

Figure 5

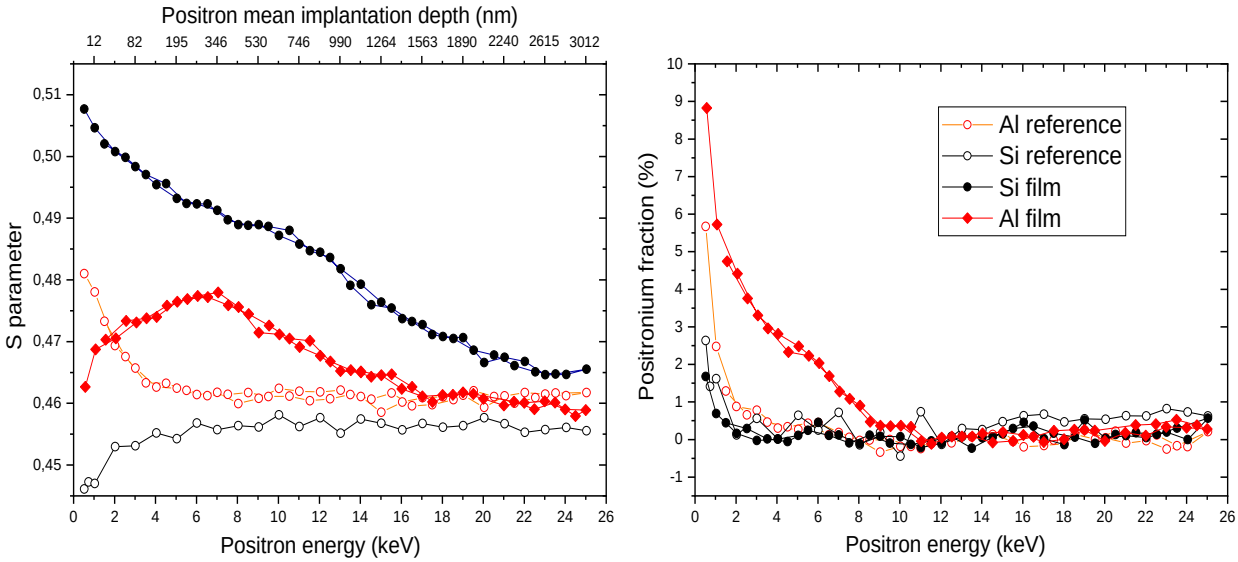
Positron mean implantation depth (nm)
12 82 195 346 530 746 990 1264 1563 1890 2240 2615 3012
S parameter
0,51
0,50
0,49
0,48
0,47
0,46
0,45
0 2 4 6 8 10 12 14 16 18 20 22 24 26
Positron energy (keV)
Positronium fraction (%)
10 9 8 7 6 5 4 3 2 1 0 -1
Al reference
Si reference
Si film
Al film
0 2 4 6 8 10 12 14 16 18 20 22 24 26
Positron energy (keV)

Figure 6

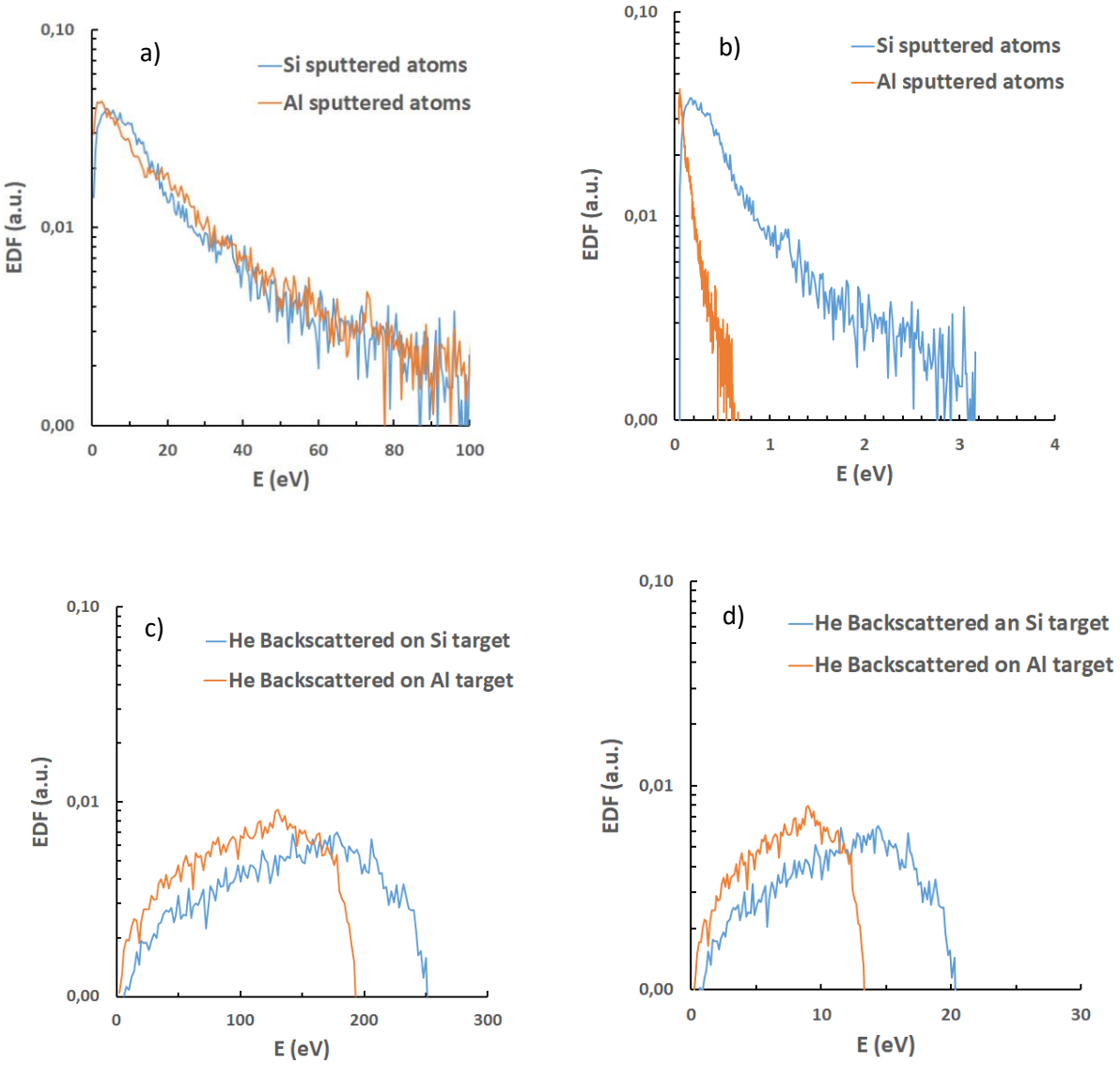
a)
Si sputtered atoms
Al sputtered atoms
EDF (a.u.)
E (eV)
b)
Si sputtered atoms
Al sputtered atoms
EDF (a.u.)
E (eV)
c)
He Backscattered on Si target
He Backscattered on Al target
EDF (a.u.)
E (eV)
d)
He Backscattered an Si target
He Backscattered on Al target
EDF (a.u.)
E (eV)

Figure 7